PNAS RESEARCH ARTICLE | ENGINEERING

Interplay of vitrification and ice formation in a cryoprotectant aqueous solution at low temperature

Christiane Alba-Simionesco[a,1], Patrick Judeinstein[a], Stéphane Longeville[a], Oriana Osta[a], Florence Porcher[a], Frédéric Caupin[b], and Gilles Tarjus[c,1]

Edited by Andrea Liu, Department of Physics & Astronomy, University of Pennsylvania, Philadelphia, PA; received July 12, 2021; accepted November 21, 2021

The proneness of water to crystallize is a major obstacle to understanding its putative exotic behavior in the supercooled state. It also represents a strong practical limitation to cryopreservation of biological systems. Adding some concentration of glycerol, which has a cryoprotective effect preventing, to some degree, water crystallization, has been proposed as a possible way out, provided the concentration is small enough for water to retain some of its bulk character and/or for limiting the damage caused by glycerol on living organisms. Contrary to previous expectations, we show that, in the "marginal" glycerol molar concentration ≈ 18%, at which vitrification is possible with no crystallization on rapid cooling, water crystallizes upon isothermal annealing even below the calorimetric glass transition of the solution. Through a time-resolved polarized neutron scattering investigation, we extract key parameters, size and shape of the ice crystallites, fraction of water that crystallizes, and crystallization time, which are important for cryoprotection, as a function of the annealing temperature. We also characterize the nature of the out-of-equilibrium liquid phases that are present at low temperature, providing more arguments against the presence of an isocompositional liquid–liquid transition. Finally, we propose a rule of thumb to estimate the lower temperature limit below which water crystallization does not occur in aqueous solutions.

aqueous solutions | nanocrystallization kinetics | out-of-equilibrium liquids | low-density amorphous water | polarized neutron scattering

Significance

Studying water crystallization at low temperature and the lower limit of ice formation is crucial both for a fundamental understanding of water and for practical reasons such as cryopreservation. By taking advantage of the polarized neutron scattering technique and by considering a nanosegregated water–glycerol solution, we are able to characterize the key parameters of ice formation at temperatures near and below the calorimetric glass transition of the solution and provide a general rule for estimating the lower temperature limit of water crystallization in a broad range of aqueous solutions. We also show that nanosegregated water in the glassy solution at low temperature is not in a high-density form but in a low-density one.

Adding glycerol to water is known to inhibit ice formation because of the perturbation that glycerol produces on the hydrogen-bonding network of water. This property has important consequences both on a practical level and on a theoretical level. Glycerol is one example of a cryoprotectant, cryoprotectants being chemicals used to protect biological molecules, organs, plants, and insects from freezing (1–9). Its addition to an aqueous solution may even allow its vitrification, provided a fast enough cooling protocol is applied, thereby opening the possibility of long-term preservation at low temperature of cells, plants, or, at a different level, protein structures (10) without the damaging interference of ice formation. On the other hand, being able to get around crystallization of water that is otherwise unavoidable in a temperature range between around 230 K and 150 K is a route to study the exciting and actively debated properties of the putative supercooled liquid water in this range (11–14).

In both cases, the concentration c_g of glycerol must somehow be optimized. Indeed, a too small concentration is not sufficient to prevent water crystallization by rapid but standard cooling techniques, whereas a too high concentration strongly perturbs water in the mixture which may then lose its resemblance to bulk water; such a high concentration then invalidates the theoretical value of the mixture as a proxy for bulk water and, on the other hand, may damage the living organisms that one is trying to preserve (1, 3, 5–9). So, one is especially interested in the lowest glycerol concentration for which glass formation is still possible by rapid cooling, say, in liquid nitrogen. It has been shown to be at least 15% in molar concentration (15–18). We have then chosen a concentration of about 18% for which, in addition, previously obtained data were available. (Here and in what follows, we use the molar concentration c_g; $c_g = 0.18$ then corresponds to a mass concentration of about 52 to 52.5%, depending on the deuteration.)

Our goal is twofold. First, we want to assess for the "marginal" concentration $c_g \approx 0.18$, at which vitrification is possible with no crystallization upon rapid cooling, the factors that characterize water crystallization and determine the cryoprotective ability of glycerol. The glass state is out of equilibrium, and, depending on how deep in it the solution is, it may undergo some form of relaxation and age, which could, in rare instances, lead to very slow crystallization. Relevant questions that have not been addressed so far are thus: What is the timescale for crystallization in this cryoprotectant aqueous solution at low temperature and how does it vary with temperature? What are the characteristics of ice formation when the

Author affiliations: [a]Laboratoire Léon Brillouin, Université Paris-Saclay, CEA, CNRS, 91191 Gif-sur-Yvette, France; [b]Institut Lumière Matière, Université de Lyon, Université Claude Bernard Lyon 1, CNRS, F-69622 Villeurbanne, France; and [c]Laboratoire de Physique Théorique de la Matière Condensée, CNRS, Sorbonne Université, 75005 Paris, France

Author contributions: C.A.-S. and G.T. designed research; C.A.-S., P.J., S.L., O.O., F.P., F.C., and G.T. performed research; C.A.-S., P.J., S.L., O.O., and F.P. analyzed data; and C.A.-S. and G.T. wrote the paper.

The authors declare no competing interest.

This article is a PNAS Direct Submission.

[1]To whom correspondence may be addressed. Email: christiane.alba-simionesco@cea.fr or tarjus@lptmc.jussieu.fr.

This article contains supporting information online at https://www.pnas.org/lookup/suppl/doi:10.1073/pnas.2112248119/-/DCSupplemental.

Published March 18, 2022.

solution is in the vicinity of its calorimetric glass transition temperature? Is there a lowest temperature below which ice can no longer appear? Second, we revisit the proposal made by Tanaka (19, 20) that an "isocompositional" liquid–liquid transition of the solution, triggered by an underlying liquid–liquid transition of water between a low-density and a high-density phase, takes place for $c_g \approx 0.18$. Although already criticized and, in our opinion, convincingly refuted by several authors (16–18), the proposal has been very recently asserted again (21), and it seems timely to add relevant experimental facts to the debate. We thus characterize the liquid phases appearing below melting, emphasizing their out-of-equilibrium character. We show, in particular, that nanosegregated water in the glassy solution at low temperature is not in a high-density amorphous (HDA) form but, rather, in a low-density one.

Our study enables us to describe the stages and the main properties of slow ice formation in a glassy environment. This may be of interest for a better understanding of ice under astrophysical conditions (comets, planets, and interstellar matter) (22). It also pertains to the broader scope of water polyamorphism and crystallization in electrolytic or nonelectrolytic aqueous solutions, a topic that has been extensively studied (for reviews see, e.g., refs. 23–25). In particular, based on the temperature dependence of the typical crystallite size that we obtain, we propose a practical way to estimate the limiting temperature below which water crystallization cannot occur for a range of aqueous solutions. The only required piece of information on the solution is its calorimetric glass transition temperature.

Before any further exposition, it is worth recalling the overall temperature–concentration phase diagram of water–glycerol solutions (15, 17–19, 26–31) (*SI Appendix*, Fig. S1). It is reasonably well established that, below melting, three different ranges of glycerol concentration should be distinguished. At low concentration, $0 < c_g \lesssim 0.15$, the presence of glycerol is not sufficient to prevent crystallization of water even by a deep quench in liquid nitrogen (alternative techniques should then be used: see, e.g., refs. 32 and 33). At high concentration, $0.28 \lesssim c_g < 1$, the cryoprotective effect of glycerol controls the thermodynamic behavior, and ice formation is easily avoided by a fast cooling; water molecules are well miscible with glycerol, and no significant phase separation takes place. Above the so-called maximally freeze concentrated solution $c_g \approx 0.38$, it is even virtually impossible to crystallize the solution, no matter how slow the cooling rate, except by introducing a crystal seed (26). Finally, the intermediate range, $0.15 < c_g \lesssim 0.28$, is the more complex and interesting one, in which a strong dependence on the thermal treatments is found. Water crystallization can be avoided by fast cooling but is then observed upon heating. It is also a range where nanosegregation may play an important role.

The core of our study is a time-resolved structural characterization of the phases and phase transformations of a water–glycerol mixture obtained after a fast quench at low temperature. This is done mostly at the glycerol concentration $c_g = 0.178 \pm 0.005$ through polarized neutron scattering and selective deuterations. An extensive set of data already exists for this concentration or nearby ones (15–19, 27, 34–36), but no detailed structural investigations have been provided so far. Through the time-resolved neutron scattering experiment, we are able to probe the kinetics of phase transformation at constant annealing temperature, which may be very long in the glassy regime (10 h or more). We further complement our analysis by thermodynamic measurements made by differential scanning calorimetry (DSC) and dynamical measurements obtained by nuclear magnetic resonance (NMR) and neutron spin echo (NSE).

Results

Water Crystallization Near and Below the Calorimetric Glass Transition of the "Marginal" Cryoprotectant Solution.

Evidence. The glass transition temperature of the fully deuterated aqueous solution with 18% of glycerol is found by DSC (cooling and heating rates of 10 K/min) at $T_g \approx 164.7$ K, that is, is about 8 K to 10 K above that of the corresponding fully hydrogenated solution (*SI Appendix*, Fig. S1). Generically, the characteristic temperatures of the deuterated sample are several degrees higher than those of the hydrogenated sample, for example, about 4 K higher for the melting temperature T_m. [The larger temperature difference for the glass transition, which is 10 K to 12 K for pure water and slowly decreases as c_g increases, stems from quantum effects observed at low temperatures (37).] We study the evolution of the static structure factor $S(Q)$ of the solution during the annealing at 160 K, that is, slightly below T_g, and at 170 K, slightly above T_g. Note that, due to the fast quench down to 80 K to 90 K (∼70 to 130 K/min), there is no sign of crystallization in the glass phase up to 160 K prior to annealing. (This is discussed in *SI Appendix*, section III. In addition, in *SI Appendix*, we provide an account of the effect of changing the cooling protocol on the results.)

We find that water crystallization takes place at 160 K, albeit at a very slow pace. Evidence is shown in Fig. 1, where the isothermal evolution over time of the static structure factor $S(Q)$ of the fully deuterated sample is plotted. The distinctive signatures of ice formation are as follows: 1) a shift of the location of the main peak to a lower wavevector, from $\sim 1.75\ \mathring{\mathrm{A}}^{-1}$ to $1.71\ \mathring{\mathrm{A}}^{-1}$; 2) a steep increase of the peak with a concomitant narrowing; 3) an increase at the lowest Q values; and 4) a strong decrease of the scattering intensity above the main peak position, around $2\ \mathring{\mathrm{A}}^{-1}$. This is even more clearly seen by looking at the difference between the data at the beginning and at the end of the annealing that is displayed in Fig. 1, *Lower Right*. These features can all be interpreted as resulting from partial crystallization of water: the peak at $1.71\ \mathring{\mathrm{A}}^{-1}$ matches the main peak of cubic ice I_c and corresponds to a broadened Bragg peak that grows as more water crystallizes; the rise at low Q is typical of the formation of interfaces, here between ice crystallites and the remaining liquid phase, and is described by Porod's Q^{-4} law; finally, the depletion around $2\ \mathring{\mathrm{A}}^{-1}$ is due to a decrease in the spatial correlations between water molecules and the alkyl chains of glycerol resulting from the formation of water crystallites. This decrease already appears when quenching the liquid into the glass, due to a nanosegregation leading to the formation of domains of pure water, but it is much more developed when water crystallizes in the domains and more water aggregates to form ice.

To complement this characterization, we also display the structure factor $S(Q)$ at the beginning and the end of the annealing for two partially deuterated samples, $C_3D_5(OH)_3 + H_2O$ and $C_3H_5(OD)_3 + D_2O$, together with the fully deuterated one, $C_3D_5(OD)_3 + D_2O$. The $S(Q)$ of $C_3D_5(OH)_3 + H_2O$ allows one to focus on the alkyl chains of glycerol which, as inferred from Fig. 1, tend to become closer as water crystallizes, with a peak in $S(Q)$ moving from about $1.05\ \mathring{\mathrm{A}}^{-1}$ to $1.2\ \mathring{\mathrm{A}}^{-1}$. One can also very clearly observe the upswing at small Qs due to the Q^{-4} Porod law associated with the interfaces formed by ice crystallites (see the analysis in *SI Appendix*, section VI). The structure factor of $C_3H_5(OD)_3 + D_2O$, for which all hydrogen atoms are deuterated except those of the alkyl chains, shows features similar to that of the fully deuterated sample. In particular, the three signatures of water crystallization, namely, the shift, growth, and narrowing of

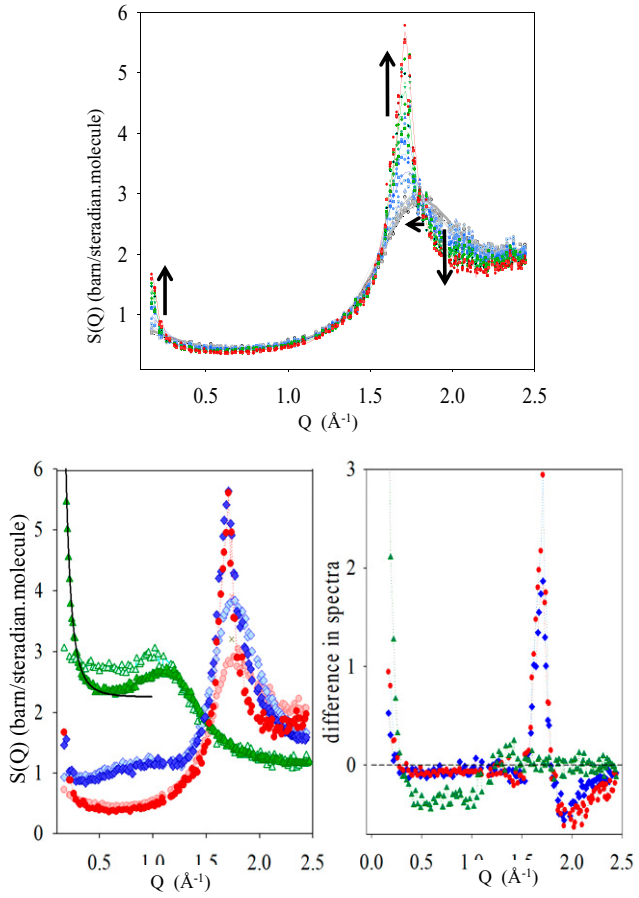

Fig. 1. (*Upper*) Evolution of the static structure factor $S(Q)$ of the fully deuterated 17.8% glycerol-rich aqueous solution during an isothermal annealing at $T = 160.2$ K, slightly below the calorimetric glass transition $T_g \approx 164.7$ K. Data are colored according to four domains of time: gray for 0 min to 176 min, then blue up to 366 min, green up to 620 min, and finally red up to 721 min. The arrows indicate the main changes with time. (*Lower Left*) Static structure factor $S(Q)$ of the fully deuterated $C_3D_5(OD)_3 + D_2O$ (red symbols) and partially deuterated $C_3D_5(OH)_3 + H_2O$ (green symbols) and $C_3H_5(OD)_3 + D_2O$ (blue symbols) $c_g = 0.178$ solution at the beginning (light color) and the end (dark color) of an isothermal annealing at $T = 160.2$ K; the dark line shows the expected Q^{-4} Porod's law at low Q (an analysis is provided in *SI Appendix*, section VI). (*Lower Right*) Same data shown as the difference between the final and the initial curves.

the main peak, the upswing at the lowest Qs, and the intensity decrease in the region around $2\,\mathrm{\AA}^{-1}$, can be distinctly seen. There are some differences between the curves of this partially deuterated sample and the fully deuterated one: This stems from differences in the prefactors weighting the contributions of the partial structure factors to the total $S(Q)$ obtained by neutron scattering; in particular, the prefactors involving hydrogen atoms are mostly negative, which, because of the overall normalization, mechanically leads to an increase of the prefactors weighting the other contributions.

All of this shows that water crystallization takes place at low temperature just below the glass transition in the presence of a molar concentration of 18% of cryoprotectant glycerol, even after a rapid quench during which no crystallization occurred. This is the main finding of our study, on which we further elaborate below. This crystallization is a consequence of the nanosegregation of the solution that leads to the formation of small domains of water, a phenomenon that is already visible in the liquid structure near the melting temperature (38). Nanosegregation of water, and its connection to ice formation, is a more general phenomenon that has also been observed, for instance, in aqueous salt solutions for a range of concentrations (39–41).

We have repeated the analysis for an annealing temperature of 170 K, slightly above the glass transition temperature. We also observe water crystallization, and the evolution is now significantly faster than at 160 K (see below). Water crystallization again appears as a first-order-like transition, as further supported by the presence of an exothermic peak in the DSC measurement (*SI Appendix*, section VII). Evidence for water (cold) crystallization at this temperature or at a higher one has already been obtained by previous authors upon heating, by DSC (17, 18, 27, 34), adiabatic calorimetry (15), X-ray scattering (19), dielectric spectroscopy (17), Raman scattering (16, 19), and infrared spectroscopy (36).

We note that the $S(Q)$'s obtained by either first annealing at 160 K followed by heating at 170 K or annealing directly at 170 K are identical (*SI Appendix*, Fig. S7). This robustness confirms that metastable states are reached at the end of the annealing times, with no further water crystallization. After heating the sample(s) to still higher temperature and taking measurements at 180, 195, 210, and 230 K, we find, as expected, that water crystallization becomes more and more prominent. In addition, the fraction of hexagonal ice, whose signature can be found in specific peaks of the structure factor, steadily increases: It is negligible (within our analysis) at 160 K, around 30% at 170 K, 42% at 180 K, almost 62% at 195 K, and 100% at 210 K and above, with no sign of a well-defined transition between I_c and I_h, contrary to what is stated in ref. 19. Note that the ice that forms at low temperature is generically expected to be a faulty cubic ice with stacks of hexagonal ice, that is, a "stacking disordered" or "stacking fault" ice (42, 43); however, the signature of I_h can only be detected in the analysis of the experimentally measured $S(Q)$ when its fraction is large enough and when the crystallites are big enough.

Crystallite size and ice fraction. Through the analysis of the neutron scattering data, we can access some of the characteristics of the ice formed in the transition.

As already described, the peak that grows at 160 K around $1.71\,\mathrm{\AA}^{-1}$ is a broadened Bragg peak of cubic ice. At 170 K, the peak is better resolved, and one sees, in addition, traces of subpeaks characteristic of hexagonal ice I_h. The broadening of the Bragg peak is, of course, due to the limited size of the ice crystallites, and, from Fig. 2, *Upper*, it is clear that crystallization of water leads to larger crystallites at 170 K than at 160 K. To get an estimate of the typical size, we have proceeded to a Rietveld analysis (44) of the data at the end of the annealing process (for both the fully deuterated $C_3D_5(OD)_3 + D_2O$ and the partially deuterated $C_3H_5(OD)_3 + D_2O$ samples, with similar outputs). The procedure is detailed in *Materials and Methods* and leads to an estimated apparent size of 4.7 ± 0.3 nm at 160 K and of 8 ± 0.5 nm at 170 K. The same analysis gives estimates of 10.5 ± 0.6 nm at 180 K and 40 nm at 195 K (Fig. 2, *Lower*).

Another feature which is potentially crucial for cryopreservation is the fraction of water that crystallizes into ice. One expects that this fraction increases with the annealing temperature. To estimate the fraction of ice in the solution, we focus on the scattered intensity at the high-Q limit of our data, near $2.5\,\mathrm{\AA}^{-1}$, whose variation reflects the decrease of water content in the solution due to ice formation (*SI Appendix*, section VIII). We find that the fraction of water that has crystallized is 21% at 160 K and 39% at 170 K.

Kinetics and timescale. The kinetics of transformation at constant temperature is followed by monitoring several quantities: the maximum of the peak of the structure factor, $S_{\max}$, the intensity at the lowest probed wavevector $Q = 0.19\,\mathrm{\AA}^{-1}$, S_{low},

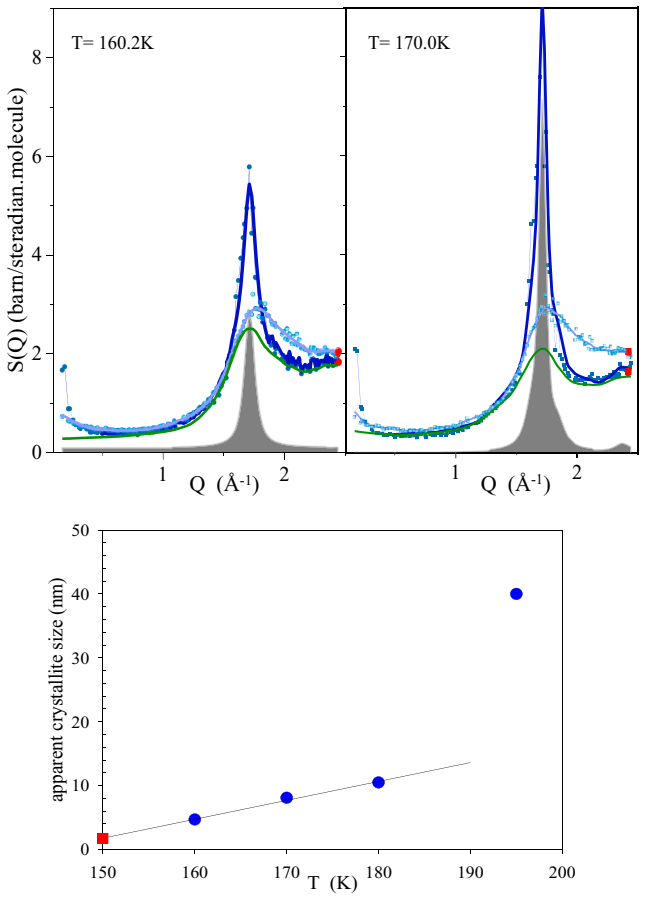

Fig. 2. (*Upper*) Rietveld analysis of the structure factor of the fully deuterated sample at $T = 160.2$ K (*Left*) and $T = 170.0$ K (*Right*). A light (dark) color indicates the initial (final) $S(Q)$; the dark blue lines correspond to the overall fit, the shaded gray peaks are the resulting crystalline contribution, and the green lines are the remaining amorphous component (cut at low Q to avoid showing the Porod regime). Finally, the red points mark the initial and final coherent cross sections at high Q. (*Lower*) Estimated apparent crystallite size as a function of the annealing temperature. The red square indicates the result of a linear extrapolation of the points at 160, 170, and 180 K down to 150 K. The line represents a linear fit of the points and allows the extrapolation to 150 K.

and the location of the main peak, $Q_{\max}$. The results for $T = 160$ and 170 K are displayed in Fig. 3. A first observation is that ice formation appears to saturate after some annealing time.

A key feature is the time needed for water crystallization, which can be read from the evolution of $S_{\max}$ and S_{low}. At 160 K, crystallization only starts after 100 min and takes around 800 min to be completed, with a typical timescale $\tau_x \sim 420$ min. The process is significantly faster at 170 K because crystallization starts after only a few minutes and is completed in less than 100 min, with a typical timescale $\tau_x \sim 37$ min. By assuming an Arrhenius temperature dependence (45–47), one then obtains an estimate for the typical timescale for crystallization of $\tau_x \sim 5{,}400$ min (i.e., almost 4 d) at 150 K.

From the transformation kinetics, we can also analyze the time dependence of the crystallized fraction $\Delta(t)$ through an Avrami fit (48, 49), $\Delta(t)/\Delta(\infty) = 1 - \exp[Kt^n]$, where $K = (1/\tau_x)^n$ depends on the temperature and on the geometry of the crystal grains, and n is the Avrami exponent that is characteristic of the growth mode (50). By fitting our data, with $\Delta(t)$ obtained from either $S_{\max}$ or S_{low} (Fig. 3), we obtain $n \approx 2.5$ to 2.7 for $T = 160$ K and $n \approx 2$ for $T = 170$ K. Note that the trend is fully compatible with the measurement done at $T = 195$ K for the same water–glycerol solution which gives an Avrami exponent of $n \approx 1.7$ (36). The value of n cannot be univocally interpreted, but, if one assumes that the nucleation rate is constant and that growth occurs by the diffusion of water molecules toward the existing grains, one can conclude that the geometry of the grains is spherical at $T = 160$ K and elongated at $T = 170$ K (50). (The latter is compatible with the more important contribution of ice I_h which tends to grow in a more anisotropic way than I_c.)

Finally, we observe that the evolution of $Q_{\max}$ (Fig. 3) is quite different from that of the crystallized fraction itself: It is much more rapid at the beginning, where it rather abruptly jumps from $\sim$1.7 to 1.71 Å^{-1}, and then stays essentially constant while growth takes off. This is the manifestation of a first stage in the transformation that consists of nucleation of (faulty) cubic ice. Growth of the grains proceeds when this first stage has been, in part, completed.

We expect that crystallization is controlled by the diffusion of water molecules, as it is for pure water (45–47, 51, 52). Below the glass transition of the solution, the glycerol-rich matrix in which nanosegregated water domains are embedded becomes very rigid as temperature further decreases, so that diffusion of water should be closer to that in a nanoconfined environment than in pure water and, therefore, even slower than in the bulk. This effect may be difficult to describe in detail, but it is tempting to

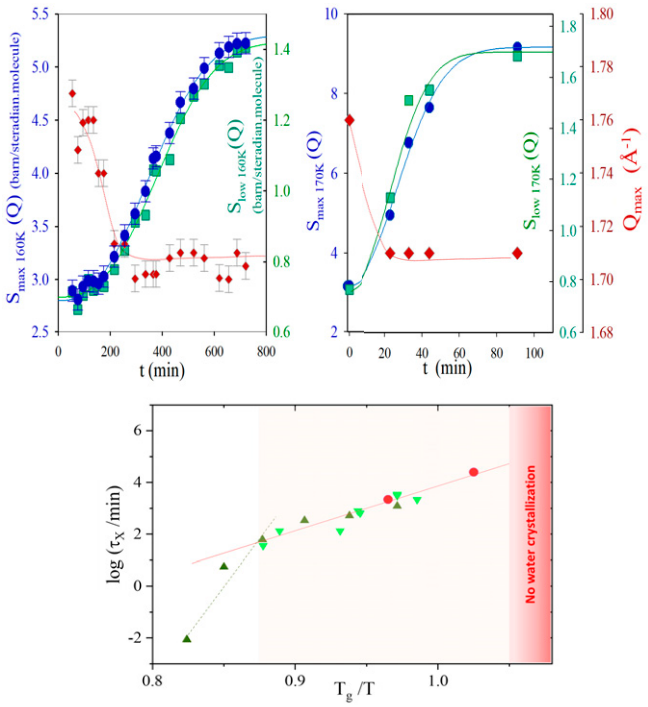

Fig. 3. (*Upper*) Crystallization kinetics at $T = 160.2$ K (*Left*) and $T = 170$ K (*Right*). The maximum of the structure factor $S_{\max}$ (blue circles) and the intensity at the lowest measured Q, S_{low} (green squares), are plotted versus time in minutes. The lines are the best fits to an Avrami formula (see the main text). We also display in both cases the evolution with time of the location $Q_{\max}$ of the main peak (red diamonds and right scale). (*Lower*) The $\log_{10}$ of the crystallization time to ice (in seconds) versus T_g/T for the $c_g = 0.178$ water–glycerol solution (red filled circles) and for either hyperquenched (45) (light green downward pointing triangles) or compressed/decompressed (53) (dark green upward pointing triangles) pure water at low temperature below 155 K (full red line and associated symbols) where temperature is rescaled by the glass transition temperature: $T_g = 164.7$ K for the fully deuterated water–glycerol solution and $T_g = 136$ K for pure water. We show, for comparison, higher temperature data for pure water (dashed green line and associated symbols), which clearly display a distinct behavior (53). Finally, the red region where no water crystallization takes place is estimated from the minimum crystallite size (see *Discussion*).

speculate that it can be accounted for at the zeroth-order level through a rescaling of the temperature by the appropriate glass transition one. Accordingly, we speculate that the dependence on the annealing temperature of the crystallization time to ice at low enough temperature, whether in pure water, water–glycerol solutions, or more generally dilute enough aqueous solutions, is controlled by the dimensionless ratio T/T_g, where T_g is the glass transition temperature of the system of interest. (This can only be valid if water is sufficiently nanosegregated in the solution and does indeed crystallize to ice; it is clearly not the case for a homogeneous solution with a high concentration of glycerol, say $c_g \gtrsim 0.28$; see *Discussion*.) To test the idea, we have plotted, in Fig. 3, *Lower*, our results for the fully deuterated $c_g \approx 0.18$ water–glycerol solution with literature data on pure water at low temperature below ∼155 K (45, 53). As can be seen from the plot, the rescaling of temperature by T_g indeed provides a very good description. We will discuss the potential benefits of this scaling below.

Evidence against an Isocompositional Liquid–Liquid Transition. A point of great fundamental interest raised by the results of Tanaka's group (19, 20) is the possibility, in a window of glycerol concentration, roughly between 15% and 20%, of an "isocompositional" liquid–liquid transition triggered by a liquid–liquid transition of water itself between a low-density and a high-density form. Strong arguments have already been given by several groups against this interpretation (16–18, 25, 54, 55), but Tanaka has reiterated his claim in a recent paper (21).

Murata and Tanaka (19, 20) acknowledge that water crystallization comes in the way of the putative liquid–liquid transition, but they consider it as an extraneous phenomenon that can be subtracted. They furthermore predict that, below a temperature T_L, which is lower than the range they studied, no crystallization should be seen, and a pristine liquid–liquid transition could be observed. For the fully hydrogenated sample with ∼18% glycerol, T_L should be around 162 K, that is, slightly above the calorimetric glass transition. With the temperature translation discussed above, one then expects a T_L of about 166 K for the fully deuterated sample. Our experiment, done with a rapid quench similar to that used in ref. 19, is thus safely below the putative T_L when annealing is considered at $T = 160$ K. The outcome, detailed above, is that, provided one is patient enough, water crystallization does take place at this temperature and explains the first-order-like transition that is observed. There is no reason to invoke an underlying liquid–liquid transition, and, even less so, an isocompositional one: With the fraction of crystallized water that we have estimated, the glycerol molar fraction of the remaining part of the sample is 21.6% at 160 K and 24.3% at 170 K, instead of the initial composition of 17.8%.

Furthermore, as we discuss below in more detail, the structure of the liquid/glass found immediately after the fast quench and that of the liquid coexisting with ice after partial water crystallization are both dominated by a low-density amorphous (LDA) form of water.

Understanding the Liquid Phases of the 18% Glycerol–Water Solution in and out of Equilibrium.

Different liquid phases out of equilibrium. The nature of the liquid phases appearing below melting at a glycerol concentration $c_g \approx 0.18$ is also a vividly debated issue. To list the main proposals: At low temperatures, it has been suggested that the system in the glass state or before any significant annealing is a homogeneous solution with water in an HDA form (19–21) or a nanosegregated solution (17), possibly with HDA water (18, 25); on the other hand, after heating and/or sufficient annealing, the proposals include a transformation to a homogeneous solution with LDA water [called liquid II (19–21)], a phase-separated system with coexistence of ice domains, interfacial water, and a water–glycerol liquid mixture close to the maximally freeze concentrated solution (17, 18, 25, 35), or a supercritical liquid fluctuating between low- and high-density forms of water and prone to crystallization (16). However, above all, one should stress that the phases observed in this temperature range are out of thermodynamic equilibrium and depend on the thermal treatment. In the following, we distinguish three liquids: liquid I, the equilibrium phase above the melting temperature T_m and the continuously related weakly supercooled liquid phase; liquid I', the (out-of-equilibrium) amorphous glass or liquid phase obtained by a fast quench of liquid I and considered prior to any significant annealing; and liquid II, the (out-of-equilibrium) liquid that remains when the ice that has formed during the annealing is (hypothetically) removed.

Liquid I' versus liquid I. Consider first liquid I'. As already mentioned, there is no sign of ice formation during the fast cooling process. However, except possibly for protocols such as hyperquenches, vapor deposition, or pressure liquid cooling vitrification (32, 33) which are not considered here, the liquid nonetheless evolves during the cooling process. Most notably, the nanosegregation which is already detected above melting (as seen from the NMR results in *SI Appendix*, section X for $c_g = 0.19$ and the computational modeling analysis for $c_g = 0.25$ in ref. 38) further develops. This can be seen by comparing the structures of liquid I and liquid I' (*SI Appendix*, Fig. S15): The main peak that is typical of water correlations moves from $1.82\,\mathring{\mathrm{A}}^{-1}$ at 260 K to $1.75\,\mathring{\mathrm{A}}^{-1}$, grows, and sharpens, while there is a drop of the intensity above $2\,\mathring{\mathrm{A}}^{-1}$ which, as already argued, denotes a decrease of correlation between water and the alkyl chains of glycerol. [Note that this is even more significant considering that, while the main peak shifts to lowers Qs, the average density increases from liquid I to liquid I' (10).] This increased nanosegregation is favored by the strong differential in mobility between water and glycerol molecules in the solution. Water becomes increasingly more mobile than glycerol when temperature decreases, as already observed over a limited range of temperature through an NMR study.

The difference between liquid I and liquid I' is also illustrated by looking at their dynamics. To characterize liquid I, we have carried out an experimental investigation by NSE in both the stable and the weakly supercooled liquid regimes. Liquid I' has already been studied by broadband dielectric spectroscopy (17, 19). We plot, in Fig. 4, the relaxation time obtained from NSE and dielectric measurements, together with viscosity data for liquid I (56), as a function of $1/T$ for $c_g \approx 0.18$ to 0.20, 0.28, and 0.40. One clearly sees that continuity of the data between liquid I at high temperature and liquid I' at low temperature is only recovered for the highest glycerol concentration shown (in this case, the liquid can be supercooled all the way from T_m to T_g). For $c_g \approx 0.18$ to 0.20 (Fig. 4, *Upper*), the dielectric results also show the abrupt changeover between liquid I' and liquid II resulting from water crystallization, which we discuss below.

The additional hallmark of liquid I', besides being nanosegregated between water domains and a glycerol richer mixture, is that, contrary to what has been stated or implied before (18–20, 25, 36), there is no trace of water being in an HDA form. To make this clear, we compare, in *SI Appendix*, Fig. S14, the $S(Q)$ that we have obtained prior to any annealing with the neutron scattering curves of LDA and HDA for pure water (57, 58). The main peak of liquid I' is not exactly at the same location as that of the LDA ($1.75\ \mathring{\mathrm{A}}^{-1}$ versus 1.69–$1.71\ \mathring{\mathrm{A}}^{-1}$), which indicates that the hydrogen bond network and local tetrahedral order are

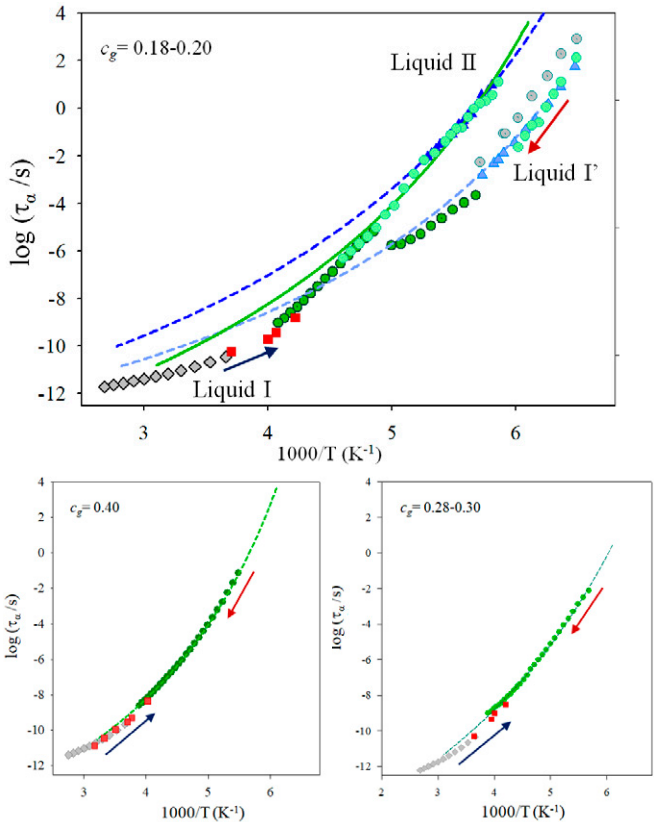

Fig. 4. Arrhenius plot of the relaxation time (in seconds) and the viscosity (rescaled to have an effective time) of the glycerol–water solution for several concentrations: (*Upper*) $c_g = 0.18$ to 0.20; NSE results ($c_g = 0.178$, red squares) are from the present study, dielectric data are from ref. 17 ($c_g = 0.20$, green circles), ref. 19 ($c_g = 0.18$, blue triangles), and ref. 35 ($c_g = 0.18$, gray circles), and viscosity is from ref. 58 ($c_g = 0.18$, gray diamonds). Dark and light shades correspond to the two protocols in refs. 17 and 19. The green full line represents dielectric results at $c_g = 0.4$ (17), and the dashed lines are fits to the low-temperature dielectric data (19). Finally, the arrows indicate whether the measurements are performed on cooling or on heating. As detailed in the text, liquid I denotes the stable and weakly supercooled liquid phase, liquid I' denotes the out-of-equilibrium amorphous phase obtained after rapid cooling and prior to ice formation, and liquid II denotes the liquid that remains when ice has formed. (*Lower Left*) The $c_g = 0.28$, except for dielectric data ($c_g = 0.30$, green circles) (17); (*Lower Right*) $c_g = 0.40$.

not as well formed and extended as in the LDA, but there is no resemblance whatsoever with the $S(Q)$ of HDA that peaks at $2.1\,\mathring{A}^{-1}$. (The same observation can be made for the X-ray diffraction pattern by comparing the data for liquid I' of ref. 19 with those for HDA and LDA in ref. 59.) Our conclusion is in line with the careful examination of the polarized Raman spectrum by Susuki and Mishima (16), contradicting a previous one by Murata and Tanaka (19), and with the analysis of liquid I at 238 K just above melting by Towey et al. (38). Note that this conclusion is compatible with the absence of a thermodynamic signature for a first-order transition between LDA and HDA in compression/decompression experiments in the glass (16, 18) if one takes into account that the domains of amorphous water are small (of the order of a nanometer): The transformation from LDA to HDA under pressure is then expected to be very gradual, with no clear signature of a transition in thermodynamic measurements.

Nature of liquid II. A final question is the nature liquid II. We have shown that water crystallization takes place even below the glass transition, provided one waits long enough, and that ice formation saturates to a given fraction that depends on the annealing temperature (for a given fast-quench protocol). Unfortunately, there is no rigorous way to subtract the contribution of ice from the measured structure factor. If one nonetheless proceeds, as first done in ref. 19 for X-ray scattering, one obtains the curves at 160 and 170 K displayed in Fig. 2, *Upper*. The remaining structure factor that is obtained after subtraction is distinct from that of liquid I' at the same temperature, but the difference is rather subtle: One finds a small shift of the main peak position from $\sim 1.75\,\mathring{A}^{-1}$ to a value of around $1.71\,\mathring{A}^{-1}$ which roughly corresponds to the peak position of the LDA (see above). Popov et al. (17) have convincingly interpreted their dielectric and DSC data as evidence for what one may call a mesoscopically phase-separated system with water appearing in three different configurations: 1) ice domains, 2) hydrogen bonded to glycerol molecules in a more-or-less water-saturated glycerol matrix, and 3) at the interface between the ice domains and the matrix. It therefore appears plausible that the shift of the main peak to a lower Q observed for the residual structure factor results from an increased contribution of a better tetrahedrally organized interfacial water as well as from the correlations between this interfacial water and the ice. The latter represents a cross-contribution that cannot be removed from the total spectrum, and the structure obtained by subtraction is thus only a proxy for that of a liquid II.

If one now considers the evolution of liquid II with increasing temperature, one must account for the fact that more water crystallization takes place. It is then unlikely that the liquid could keep the same composition, be it the original one (19–21) or the maximally freeze concentrated one (17, 18, 25). Actually, as seen in Fig. 4, *Upper* for $c_g \approx 0.18$ to 0.20, there is a clear signature of the sudden change between liquid I' and liquid II, a change that is a consequence of the partial crystallization of water in the solution. However, upon slow heating, the T dependence of the dielectric relaxation time of the latter departs more and more from the curve of the 30 to 40% concentrated mixture to finally meet that of liquid I at high enough temperature. Liquid II is thus an out-of-equilibrium phase, resulting from the transformation of water into ice, and whose nature evolves with temperature.

Discussion

In addition to a better understanding of the nature of the phases formed out of equilibrium by reheating rapidly quenched water–glycerol solutions and of the interplay between vitrification and ice formation, the present study brings some lessons for cryoprotection. First, we show that, even a few degrees below the calorimetric glass transition, slow water crystallization occurs in an aqueous solution with 18% glycerol; this takes place on a timescale of the order of 10 h, after which ice formation saturates. Second, we are able to estimate, for this solution, key parameters that control the potentially damaging effects of ice formation—size and shape of the ice crystallites, fraction of water converted to ice, and crystallization time—as a function of the annealing temperature. We find, by extrapolating our data, that annealing the solution at a still lower temperature, say of 10 K below the lowest one we have studied (160 K in the present case), would lead to a strong increase of the crystallization time that could reach almost 4 d. However, such a time may not be long enough for long-term cryopreservation.

This leads us to take a different angle on the question of the lower temperature limit for water crystallization. Rather than envisaging time as being the limiting factor, one should consider the typical size of the ice crystallites. It has been shown, by a combination of experimental and simulation techniques, that ice I no longer appears when the ice clusters contain less than 90

molecules at 150 K (and 70 molecules at ∼100 K) (60). This corresponds to a size (diameter) of about 1.6 nm to 1.7 nm. Using a linear extrapolation of the last three data points in Fig. 2, *Lower* (red square) gives an estimate for the crystallite size of about 1.7 ± 0.1 nm at 150 K. This strongly suggests that ice can no longer form at this temperature.

We now propose to combine this finding with the speculation discussed above, that the temperature dependence of water crystallization in dilute aqueous solutions is controlled by the dimensionless ratio T/T_g, to provide a rule of thumb for estimating the lowest temperature at which water crystallization can happen in such an aqueous solution: Multiply the ∼150 K estimated here by the ratio of the T_g of the chosen aqueous solution and the T_g of the fully deuterated 18% glycerol–water solution, that is, 165 K: $T_{\mathrm{lowest}}(\mathrm{solution}) \approx (150/165)\ T_g(\mathrm{solution})$. Note, as a cross-check of the soundness of this relation, that it predicts that the lower temperature limit for ice formation in pure water is ∼124 K, a temperature that seems, indeed, quite reasonable (45, 47, 57).

What is the range of aqueous solutions to which this rule of thumb may apply? First, although we have focused on cryoprotectant solutions in which organic nonionic molecules such as glycerol are added to water, electrolytic solutions of water and salt which have been extensively studied are also concerned. Second, the solution should be dilute enough so that water at low temperature is nanosegregated and/or retains some of its bulk characteristics. To get a rough estimate of the upper solute concentration below which this would hold, one could 1) extrapolate the line of homogeneous nucleation of ice and determine when it crosses the glass transition line (3, 61), 2) locate the crossover concentration at which the (positive) difference between the macroscopic density of the glass and that of the liquid above melting starts to rapidly decrease as concentration further decreases (10), or 3) use structural indicators such that the presence of a rise in the low-Q part of the structure factor below $0.4\ \mathring{\mathrm{A}}^{-1}$ and/or of a shift of the main peak to lower Qs (toward the LDA location) upon quenching the solution to a glass. The usefulness of the latter criterion, which requires that the main peak is sufficiently sensitive to the correlations among water molecules, may depend on the details of the solution: For small solute molecules such as ethylene glycol, other contributions involving the solute may be involved, which obscures the behavior of water, and, for ionic solutions, one has to take into account the specific organization of water in solvation shells around the ions. For water–glycerol solutions, the above criteria all seem to restrict the range to $c_g \lesssim 0.21$–0.22 (*SI Appendix*, Fig. S1 and section I). For the salt solution of LiCl in water, the upper bound would be a molar concentration of around 12% from criterion 1 (23, 24) and 16% from criterion 2 (62). The rule of thumb for, say, a 10% solution then predicts that no ice formation is possible below $T_{\mathrm{lowest}} \approx (150/165)139 \approx 126$ K. More investigations are certainly necessary to refine the prediction and the range of solutions to which it applies.

As far as cryopreservation is concerned, preventing ice formation is one prerequisite. One should also be able to heat back the sample at room temperature without too much damage caused by ice formation and thawing during the heating process. Considering what we have found in the present study, this seems hard to avoid with a simple glycerol–water solution in the "marginal" concentration range. Other chemicals such as ice recrystallization inhibitors would then be required (63, 64). The knowledge of the crystallite size and shape and of the fraction of ice, as provided in the present study, are then potentially crucial to design the appropriate cryoprotectant mixtures.

Materials and Methods

Samples. Thanks to the neutron scattering method, the contribution of partial structure factors can be selectively probed through specific H/D substitutions. The isotopic compositions were chosen in such a way that there was no exchange between H and D during the different thermal treatments nor any uncertainties in the analysis of the scattering data. The sample compositions used for elastic neutron scattering are summarized in *SI Appendix*, Table S1 and detailed below in the sections about DSC and NSE. The sample concentration c_g is expressed as the number of glycerol molecules divided by the total number of molecules. The samples were purchased from Sigma-Aldrich, Eurisotop, and Cambridge Isotope Laboratory and used without any further purification. The deuteration rate is 99.9% for D_2O, 99.9% for fully deuterated glycerol, and above 98% for partly deuterated glycerol.

Polarized Neutron Scattering Experiments. The neutron scattering experiments were performed on the D7 spectrometer at the Institut Laue Langevin (ILL) in Grenoble (France). The main advantage of this instrument is its ability to separate coherent scattering (containing the structural information) from incoherent scattering by using a technique of longitudinal neutron polarization analysis (65). The incoherent scattering can be used as an internal calibration. In this way, one directly obtains the coherent scattering signal in absolute units [barn/(steradian.molecule)] and one avoids "vanadium calibration" of the instrument with all its uncertainties. We considered one glycerol concentration, $c_g \approx 0.18$, but several H/D substitutions, with D_2O or H_2O and fully [$C_3D_5(OD)_3$] or partially deuterated [$C_3H_5(OD)_3$ and $C_3D_5(OH)_3$] glycerol, were used to independently focus on the contribution of water, of atoms involved in a hydrogen bond network, and of the alkyl chains. We verified, for each of the mixtures, that the measured *S(Q)* at high *Q* in liquid I′ prior to any crystallization is fully compatible with the calculated total coherent scattering cross-section per steradian and per molecule. The former values were used as a basis to estimate the amount of crystallized water and the glycerol mole fraction of the remaining solution without ice (*SI Appendix*, section VIII).

Measurements were performed from 130 K to 300 K in an Orange cryostat by using an aluminum annular cell of 0.2-mm thickness and an external diameter of 19.5 mm in order to maximize the transmission. A wavelength of 4.8 Å was chosen to measure the structure factor in the *Q* range $0.1\ \mathring{\mathrm{A}}^{-1} < Q < 2.4\ \mathring{\mathrm{A}}^{-1}$. The raw data obtained on D7, that is, measurements of the non–spin flip scattered intensity and the spin flip one, were corrected by using the standard reduction software developed at the ILL (https://www.ill.eu/users/instruments/instruments-list/d7/characteristics). The data are first normalized by the monitor counts. The background, measured from the scattering of the empty cell and a dark sample (cadmium) with the same geometry, was subtracted after taking into account the appropriate self-absorption corrections (i.e., the measured transmission of the sample). The flipping ratio was measured from a quartz rod of the same diameter, and the detectors' efficiency was corrected with a vanadium sample. The incoherent and coherent signals were then calculated from the non–spin flip and spin flip scattered intensities. Absorption and multiple scattering were kept negligible by ensuring, with a high transmission, that only a few percent of the neutrons were scattered and by choosing cylindrical sample geometry (of only 0.2-mm thickness). Thanks to the method, inelastic events included in the incoherent scattering were properly subtracted.

Complementary structural investigations were performed at the Laboratoire Léon Brillouin (LLB) on the instrument G44 (see https://www-llb.cea.fr/fr-en/pdf/g44-llb.pdf) which provides an increased *Q* range at the expense of a lower flux and no neutron polarization. Experiments then take longer. A wavelength of 2.89 Å and a cylindrical vanadium cell of 6-mm diameter were used. Results are illustrated for $c_g = 0.28$ in *SI Appendix*, section XI.

Rietveld Analysis. The Rietveld method allows an easy modeling of the peak shape, width, and intensity of diffraction patterns in relation to the atomic structure of crystalline phases and their relative contribution (44). The Rietveld analysis of the polarized neutron scattering data was performed with the FullProf program (see https://www.ill.eu/sites/fullprof/ and ref. 66). The refinement of the scattered intensities was carried out as a function of the scattering angle 2θ, which is the experimental quantity for a monochromatic diffractometer as D7 (the wave vector *Q* is then defined as $Q = 4\pi \sin\theta/\lambda$, where the wavelength λ is 4.8 Å), by

accounting for the instrumental resolution as detailed in ref. 67. The peak intensity and shape were fitted by taking into account an averaged crystal structure based on the hexagonal I_h and cubic I_c crystalline structures of pure D_2O (68, 69) and their possible combination. The sharpening of the peak with increasing annealing time and/or temperature provides a measure of the average (isotropic) crystallite size. Finally, the difference between the experimental data and the pattern calculated from the structural model corresponds to the averaged residual amorphous part present in the sample. In summary, this analysis gives access to the proportion of hexagonal and cubic ice, to the average size of the crystallites, and to the remaining amorphous or liquid contribution.

NSE and Neutron Resonance Spin Echo. NSE is a powerful quasi-elastic neutron scattering technique to study the dynamical properties of the mixtures in a wide momentum transfer range and in the range of a few picoseconds to tens of nanoseconds (70). NSE is based on the neutron spin property (its spin rotation) which encodes the energy transfer occurring during the scattering process. Before and after the process, a magnetic field is applied which generates the precession of the neutron and only depends on the velocity difference of each neutron, irrespective of the initial velocity. As a result, this difference is independent of the chosen wavelength, which means that NSE can use a wide distribution of wavelength while keeping its resolution and boosting the signal intensity. The outcome is the normalized intermediate scattering function *F(Q,t)*; it contains the contributions from both coherent and incoherent functions. However, in a fully deuterated sample, the coherent part can be easily extracted, which gives access to the collective component of the correlation function.

The instrument MUSES at the LLB (Saclay, France) combines conventional and neutron resonance spin echo (NRSE) (71, 72). The conventional NSE spectrometer is used for measurements at small (so-called Fourier) times ($t < 200$ ps), and the NRSE option gives access to measurements at longer times (200 ps $< t <$ 2,000 ps). The experiments are carried out with an energy resolution of 0.3 μeV with an incident neutron spectrum of $\delta\lambda/\lambda = 0.15$ bandwidth. We studied fully deuterated samples with several glycerol mole fractions, $c_g = 0.178$, 0.28, 0.40, to cover the whole domain II of the phase diagram in *SI Appendix*, Fig. S1. Typical curves are shown in *SI Appendix*, Fig. S11 for $c_g = 0.178$ and several temperatures from 200 K to 280 K at the wave vector $Q = 1.9$ Å^{-1} corresponding to the maximum of the structure factor $S(Q)$ in this range of temperature.

DSC. DSC is a thermal analysis that measures the heat flow associated with materials transitions as a function of the time and temperature, in a controlled atmosphere. In the present case, DSC with a cooling rate and a heating rate of 10 K/min was used to determine the temperature of the glass transition of the deuterated samples as well as their melting/freezing phase transitions plotted in *SI Appendix*, Fig. S1. No signature of crystallization was observed when cooling at 10 K/min (crystallization only occurred on heating); however, crystallization was observed upon cooling at a rate of 2 K/min. DSC scans are shown in *SI Appendix*, section VII.

High-Resolution and Pulsed Field Gradient ^{1}H NMR. The NMR sample was prepared with fully protonated glycerol and water at a molar fraction $c_g = 0.19$. The mixture was immediately sealed in a glass tube of 4-mm diameter. NMR spectra were recorded with a Bruker Avance spectrometer at 9.4 T (^{1}H resonance frequency: 400.13 MHz) and a standard dual broadband 5-mm probehead equipped with a gradient coil. A Bruker temperature controller unit using evaporated liquid nitrogen flow allows experiments between 180 and 330 K with an accuracy and stability of ±2 K. Temperature calibration was performed with a standard methanol reference tube. Measurement of the area of the different signals gives access to the ratio of mobile and immobile species in the sample, hence to the fraction of crystallized water (73).

Self-diffusion coefficients were measured by pulsed field gradient NMR and stimulated echo sequence (74). The maximum magnitude of the pulsed field gradient was 60 G × cm^{-1}, the diffusion delay Δ was adjusted between 50 and 1,000 ms, and the gradient pulse length δ was set between 1 and 5 ms, depending on the diffusion coefficient. The self-diffusion coefficients were determined from the classical Stejskal–Tanner equation (75), $\ln(I/I_0) = -DG^2\gamma^2\delta^2(\Delta - \delta/3)$, where G is the magnitude of the two applied gradient pulses, γ is the gyromagnetic ratio of the nucleus under study, and I and I_0 are the integrated intensities of the signal obtained with and without gradient pulses, respectively. Here, we used 16 equally spaced gradient steps for each experiment. Data acquisition and treatment were performed with the Bruker Topspin software.

Thermal Treatments. For the structural studies, we quenched the liquid samples in liquid nitrogen from 295 K down to 80 K to 90 K. This roughly corresponds to a cooling rate of 70 K/min to 130 K/min. The sample temperature was fully stabilized at 90 K and then taken at 130 K, at which measurements were performed to characterize the glass phase. The samples were further heated to the chosen annealing temperature close to the glass temperature (i.e.,160 and 170 K), and we followed the evolution of the structure for long annealing times until the signal was completely stabilized. To give an idea, this took around 13 h at 160 K. Finally, we further heated the sample. We also studied another protocol corresponding to a slow cooling of 3 K/min to 6 K/min down to the glass at 130 K. We then heated the sample to the temperature at which the measurements were performed (*SI Appendix*, section IV).

Data Availability. All study data are included in the article and/or *SI Appendix*.

ACKNOWLEDGMENTS. We thank I. Popov and Y. Feldman for fruitful discussions and access to their dielectric data, A. Wildes, who was the local contact on D7 at the ILL, M. Hartmann for discussion on the structural data, F. Legendre for technical support at the LLB (MUSES), and M. Bombled for helping on the DSC experiments at the LLB. We also thank the Équipe de Résonance Magnétique Nucléaire (eRMN) team of Institut de Chimie Moléculaire et des Matériaux d'Orsay at University Paris-Saclay for providing access to the NMR facility, and J. Teixeira for useful exchanges and a careful reading of the manuscript.

1. C. Polge, A. U. Smith, A. S. Parkes, Revival of spermatozoa after vitrification and dehydration at low temperatures. *Nature* **164**, 666 (1949).
2. J. Farrant, Mechanism of cell damage during freezing and thawing and its prevention. *Nature* **205**, 1284–1287 (1965).
3. G. M. Fahy, D. R. MacFarlane, C. A. Angell, H. T. Meryman, Vitrification as an approach to cryopreservation. *Cryobiology* **21**, 407–426 (1984).
4. G. M. Fahy *et al.*, Physical and biological aspects of renal vitrification. *Organogenesis* **5**, 167–175 (2009).
5. K. E. Zachariassen, E. Kristiansen, Ice nucleation and antinucleation in nature. *Cryobiology* **41**, 257–279 (2000).
6. B. J. Fuller, Cryoprotectants: The essential antifreezes to protect life in the frozen state. *Cryo Lett.* **25**, 375–388 (2004).
7. M. Wisniewski, L. Gusta, G. Neuner, Adaptive mechanisms of freeze avoidance in plants: A brief update. *Environ. Exp. Bot.* **99**, 133–140 (2014).
8. J. J. Stachecki, "Vitrification : Methods contributing to successful cryopreservation outcomes" in *In Vitro Fertilization*, Z. Nagy, A. Varghese, A. Agarwal, Eds. (Springer, Cham, 2019), pp. 665–674.
9. G. M. Fahy, B. Wowk, "Principles of ice-free cryopreservation by vitrification" in *Cryopreservation and Freeze-Drying Protocols*, W. F. Wolkers, H. Oldenhof, Eds. (Methods in Molecular Biology, Springer, New York, 2015), **vol. 1257**, pp. 21–82.
10. C. Shen *et al.*, Thermal contraction of aqueous glycerol and ethylene glycol solutions for optimized protein-crystal cryoprotection. *Acta Crystallogr. D Struct. Biol.* **72**, 742–752 (2016).
11. O. Mishima, L. D. Calvert, E. Whalley, An apparent first-order transition between two amorphous phases of ice induced by pressure. *Nature* **314**, 76–78 (1985).
12. O. Mishima, H. E. Stanley, The relationship between liquid, supercooled and glassy water. *Nature* **396**, 329–335 (1998).
13. P. H. Poole, F. Sciortino, U. Essmann, H. E. Stanley, Phase behaviour of metastable water. *Nature* **360**, 324–328 (1992).
14. P. G. Debenedetti, Supercooled and glassy water. *J. Phys. Condens. Matter* **15**, R1669–R1726 (2003).
15. A. Inaba, O. Andersson, Multiple glass transitions and two step crystallization for the binary system of water and glycerol. *Thermochim. Acta* **461**, 44–49 (2007).
16. Y. Suzuki, O. Mishima, Experimentally proven liquid-liquid critical point of dilute glycerol-water solution at 150 K. *J. Chem. Phys.* **141**, 094505 (2014).
17. I. Popov, A. Greenbaum Gutina, A. P. Sokolov, Y. Feldman, The puzzling first-order phase transition in water-glycerol mixtures. *Phys. Chem. Chem. Phys.* **17**, 18063–18071 (2015).
18. J. Bachler *et al.*, Glass polymorphism in glycerol-water mixtures: II. Experimental studies. *Phys. Chem. Chem. Phys.* **18**, 11058–11068 (2016).
19. K. Murata, H. Tanaka, Liquid-liquid transition without macroscopic phase separation in a water-glycerol mixture. *Nat. Mater.* **11**, 436–443 (2012).
20. K. Murata, H. Tanaka, General nature of liquid-liquid transition in aqueous organic solutions. *Nat. Commun.* **4**, 2844 (2013).
21. H. Tanaka, Liquid-liquid transition and polyamorphism. *J. Chem. Phys.* **153**, 130901 (2020).
22. P. Jenniskens, D. F. Blake, Crystallization of amorphous water ice in the solar system. *Astrophys. J.* **473**, 1104–1113 (1996).
23. C. A. Angell, E. J. Sare, J. Donnella, D. R. MacFarlane, Homogeneous nucleation and glass transition temperatures in solutions of Li salts in D_2O and H_2O. Doubly unstable glass regions. *J. Phys. Chem.* **85**, 1461–1464 (1981).

24. C. A. Angell, Liquid fragility and the glass transition in water and aqueous solutions. *Chem. Rev.* **102**, 2627–2650 (2002).
25. J. Bachler, P. H. Handle, N. Giovambattista, T. Loerting, Glass polymorphism and liquid-liquid phase transition in aqueous solutions: Experiments and computer simulations. *Phys. Chem. Chem. Phys.* **21**, 23238–23268 (2019).
26. L. Lane, Freezing points of glycerol and its aqueous solutions. *Ind. Eng. Chem.* **17**, 924 (1925).
27. D. Harran, Comportement thermique et courbe de transition vitreuse du binaire glycérol-eau [in French]. *Bull. Soc. Chim. Fr.* **1–2**, 40–44 (1978).
28. K. Miyata, H. Kanno, Supercooling behavior of aqueous solutions of alcohols and saccharides. *J. Mol. Liq.* **119**, 189–193 (2005).
29. M. H. Jensen, C. Gainaru, C. Alba-Simionesco, T. Hecksher, K. Niss, Slow rheological mode in glycerol and glycerol-water mixtures. *Phys. Chem. Chem. Phys.* **20**, 1716–1723 (2018).
30. H. Nakagawa, T. Oyama, Molecular basis of water activity in glycerol-water mixtures. *Front Chem.* **7**, 731 (2019).
31. B. Malfait, A. Pouessel, A. Jani, D. Morineau, Extension and limits of cryoscopy for nanoconfined solutions. *J. Phys. Chem. Lett.* **11**, 5763–5769 (2020).
32. Y. Suzuki, S. Takeya, Slow crystal growth of cubic ice with stacking faults in a lassy dilute glycerol aqueous solution. *J. Phys. Chem. Lett.* **11**, 9432–9438 (2020).
33. Y. Suzuki, Non-segregated crystalline state of dilute glycerol aqueous solution. *J. Chem. Phys.* **152**, 144501 (2020).
34. Y. Hayashi, A. Puzenko, Y. Feldman, Ice nanocrystals in glycerol-water mixtures. *J. Phys. Chem. B* **109**, 16979–16981 (2005).
35. L.-S. Zhao, Z.-X. Cao, Q. Wang, Glass transition of aqueous solutions involving annealing-induced ice recrystallization resolves liquid-liquid transition puzzle of water. *Sci. Rep.* **5**, 15714 (2015).
36. J. R. Bruijn, T. H. van der Loop, S. Woutersen, Changing hydrogen-bond structure during an aqueous liquid-liquid transition investigated with time-resolved and two-dimensional vibrational spectroscopy. *J. Phys. Chem. Lett.* **7**, 795–799 (2016).
37. C. Gainaru *et al.*, Anomalously large isotope effect in the glass transition of water. *Proc. Natl. Acad. Sci. U.S.A.* **111**, 17402–17407 (2014).
38. J. J. Towey, A. K. Soper, L. Dougan, Low-density water structure observed in a nanosegregated cryoprotectant solution at low temperatures from 285 to 238 K. *J. Phys. Chem. B* **120**, 4439–4448 (2016).
39. L. Le, V. Molinero, Nanophase segregation in supercooled aqueous solutions and their glasses driven by the polyamorphism of water. *J. Phys. Chem. A* **115**, 5900–5907 (2011).
40. G. Bullock, V. Molinero, Low-density liquid water is the mother of ice: On the relation between mesostructure, thermodynamics and ice crystallization in solutions. *Faraday Discuss.* **167**, 371–388 (2013).
41. P. D. Lane *et al.*, Experimental observation of nanophase segregation in aqueous salt solutions around the predicted liquid-liquid transition in water. *Phys. Chem. Chem. Phys.* **22**, 9438–9447 (2020).
42. T. C. Hansen, M. M. Koza, W. F. Kuhs, Formation and annealing of cubic ice: I. Modelling of stacking faults. *J. Phys. Condens. Matter* **20**, 285104 (2008).
43. E. B. Moore, V. Molinero, Is it cubic? Ice crystallization from deeply supercooled water. *Phys. Chem. Chem. Phys.* **13**, 20008–20016 (2011).
44. H. M. Rietveld, A profile refinement method for nuclear and magnetic structures. *J. Appl. Cryst.* **2**, 65–71 (1969).
45. W. Hage, A. Hallbrucker, E. Mayer, Crystallization kinetics of water below 150 K. *J. Chem. Phys.* **100**, 2743–2747 (1994).
46. E. B. Moore, V. Molinero, Ice crystallization in water's "no-man's land." *J. Chem. Phys.* **132**, 244504 (2010).
47. Y. Xu, N. G. Petrik, R. S. Smith, B. D. Kay, G. A. Kimmel, Growth rate of crystalline ice and the diffusivity of supercooled water from 126 to 262 K. *Proc. Natl. Acad. Sci. U.S.A.* **113**, 14921–14925 (2016).
48. M. Avrami, Kinetics of phase change. I. *J. Chem. Phys.* **7**, 1103–1112 (1939).
49. M. Avrami, Kinetics of phase change. II. *J. Chem. Phys.* **8**, 212–224 (1940).
50. P. Papon, J. Leblond, P. H. E. Meijer, *The Physics of Phase Transitions: Concepts and Applications* (Springer, Berlin, 2002).
51. W. Hage, A. Hallbrucker, E. Mayer, G. P. Johari, Kinetics of crystallizing D_2O water near 150 K by Fourier-transform infrared-spectroscopy and a comparison with the corresponding calorimetric studies on H_2O water. *J. Chem. Phys.* **103**, 545–550 (1995).
52. R. Scott Smith, C. Huang, B. D. Kay, Evidence for molecular translational diffusion during the crystallization of amorphous solid water. *J. Phys. Chem. B* **101**, 6123–6126 (1997).
53. C. Lin, J. S. Smith, S. V. Sinogeikin, G. Shen, Experimental evidence of low-density liquid water upon rapid decompression. *Proc. Natl. Acad. Sci. U.S.A.* **115**, 2010–2015 (2018).
54. A. Puzenko *et al.*, Relaxation dynamics in glycerol-water mixtures: I. Glycerol-rich mixtures. *J. Phys. Chem. B* **109**, 6031–6035 (2005).
55. A. Puzenko, Y. Hayashi, Y. Feldman, Space and time scaling in glycerol-water mixtures. *J. Non-Cryst. Solids* **353**, 4518–4522 (2007).
56. J. B. Segur, H. E. Oberstar, Viscosity of glycerol and its aqueous solutions. *Ind. Eng. Chem.* **43**, 2117–2120 (1951).
57. M. M. Koza, H. Schober, H. E. Fischer, T. Hansen, F. Fujara, Kinetics of the high- to low-density amorphous water transition. *J. Phys. Condens. Matter* **15**, 321–332 (2003).
58. M.-C. Bellissent-Funel, J. Texeira, L. Bosio, Structure of high-density amorphous water. II. Neutron scattering study. *J. Chem. Phys.* **87**, 2231–2235 (1987).
59. J. Urquidi *et al.*, Isotopic quantum effects on the structure of low density amorphous ice. *J. Phys. Condens. Matter* **15**, 3657–3664 (2003).
60. D. R. Moberg *et al.*, The end of ice I. *Proc. Natl. Acad. Sci. U.S.A.* **116**, 24413–24419 (2019).
61. W. F. Rall, G. M. Fahy, Ice-free cryopreservation of mouse embryos at −196°C by vitrification. *Nature* **313**, 573–575 (1985).
62. A. Elarby-Aouizerat *et al.*, Metastable crystallization products and metastable phase diagram of the glassy and supercooled aqueous ionic solutions of LiCl. *J. Non-Cryst. Solids* **104**, 203–210 (1988).
63. P. L. Davies, J. Baardsnes, M. J. Kuiper, V. K. Walker, Structure and function of antifreeze proteins. *Philos. Trans. R. Soc. Lond. B Biol. Sci.* **357**, 927–935 (2002).
64. C. Budke *et al.*, Quantitative efficacy classification of ice recrystallization inhibition agents. *Cryst. Growth Des.* **14**, 4285–4294 (2014).
65. J. R. Stewart *et al.*, Disordered materials studied using neutron polarization analysis on the multi-detector spectrometer D7. *J. Appl. Cryst.* **42**, 69–84 (2009).
66. J. Rodríguez-Carvajal, "Neutron diffraction from polycrystalline materials" in *Lecture Notes of the First Summer School on Neutron Scattering*, A. Furrer, Ed. (Paul Scherrer Institut Proceedings, 1993), pp. 73–95.
67. T. Fennell, L. Mangin-Thro, H. Mutka, G. J. Nilsen, A. R. Wildes, Wavevector and energy resolution of the polarized diffuse scattering spectrometer D7. *Nucl. Instrum. Methods Phys. Res. A* **857**, 24–30 (2017).
68. S. W. Peterson, H. A. Levy, A single-crystal neutron diffraction study. *Acta Cryst.* **10**, 70–76 (1957).
69. J. P. Arnold, E. D. Finch, S. W. Rabideau, R. G. Wenzel, Neutron-diffraction study of ice polymorphs. III. Ice Ic. *J. Chem. Phys.* **49**, 4365–4369 (1968).
70. F. Mezei, Neutron spin-echo–new concept in polarized thermal neutron techniques. *Z. Phys.* **255**, 146–160 (1972).
71. M. Koeppe *et al.*, Performance and future of a neutron resonance spin echo spectrometer. *J. Neutron Res.* **4**, 261–273 (1996).
72. S. Longeville, Neutron spin echo spectrometry with zero field or by resonance. *J. Phys. IV France* **10**, 59–75 (2000).
73. N. Buchtová *et al.*, Water dynamics in silanized hydroxypropyl methylcellulose based hydrogels designed for tissue engineering. *Carbohydr. Polym.* **202**, 404–408 (2018).
74. W. S. Price, *NMR Studies of Translational Motion: Principles and Applications* (Cambridge University Press, 2009).
75. E. O. Stejskal, J. E. Tanner, Spin diffusion measurements: Spin echoes in the presence of a time-dependent field gradient. *J. Chem. Phys.* **42**, 288–292 (1965).